Journal of Materials Chemistry A

Accepted Manuscript

ROYAL SOCIETY OF CHEMISTRY

www.rsc.org/materialsA

Journal of Materials Chemistry A

ARTICLE

Layered Metal-Organic Framework/Graphene Nanoarchitectures for Organic Photosynthesis under Visible Light

Received 00th January 20xx,
Accepted 00th January 20xx

DOI: 10.1039/x0xx00000x

www.rsc.org/

Jie Xu, Sha He, Hualei Zhang, Jiancai Huang, Huaxiang Lin, Xuxu Wang, Jinlin Long*

A layered nanoarchitecture composed of photoactive MOFs of UiO-66-NH_2 and graphene was facilely fabricated herein by an innovative strategy, which utilizes a noncovalent methodology for graphene functionalization combined with *in-situ* self-assembling and solvothermal synthesis technique. The fabricated hybrids were detailedly characterized and evaluated by the selective photocatalytic oxidation of benyl alcohol under visible light. The hybrid displayed the improved efficiency at high selectivity, compared with the parent MOF. The characterization results clearly demonstrate that it is origianted from the sandwich-like hierarchical nanoarchitecture formed by the compact interaction between UiO-66-NH_2 and graphene via the adopted mediater. The synthesis strategy was also proved effective in building the rGO/NH_2-MIL-125(Ti) hierarchical nanoarchitecture. Thus, this work offers a general strategy for constructing MOFs/graphene sandwich heterostructures, which owns great potential in the fields of electronics, optics, optoelectronics, and photoconversion.

Introduction

Vertical integration of two-dimensional (2D) sheet materials and other frameworks to build hierarchical nanoarchitectures by intelligent layer-by-layer stacking has long been employed to endow them novel features, in particular of which are fascinating electronic and optoelectronic properties. Recently, in the scientific community, intense interests have been focused on metal dichalcogenide[1-5], graphene and graphene-based materials[6-14]. Owing to high mechanical strength and chemical stability as well as low electrical resistivity, graphene and its counterparts including graphene oxide (GO) and nitrogen-doped graphene, etc., have been demonstrated excellent supports or cocatalysts or catalysts to build various nanoarchitectures and catalyze specific reactions[15-18]. Their hybridization with various nanocrystals including noble metals, metal oxides and sulfides, and metal coordination compounds has been proven effective in achieving enhanced physicochemical properties and creating novel chemical functions, ranging from gas absorption, field-effect transistor, electronics, photovoltaic devices, memory devices to catalysis and photocatalysis[19-23].

As a large class of crystalline porous materials, metal-organic frameworks (MOFs) have gained growing attention over the past decade. Owning to the unique physicochemical properties, including high surface areas and porosity, well-defined porous texture, structural flexibility, diversiform composition, and good stability in both chemical and thermal environment, MOFs have showed tremendous applications in numerous fields, such as catalysis, gas storage and separation, molecular sensing, drug delivery, bioimaging, electronics, photovoltaic device, photocatalysis, and so on[24-29]. However, in terms of the utilization efficiency in each field, especially catalysis, electronics, photovoltaics and photocatalysis, it is undisputedly imperative to achieve functionalized MOFs with enhanced performance. Post-modification can not only modulate the electrical, structural, and morphological characteristics of MOFs, but features them exciting functions, among which assembling with other materials is one of the effectual ways. Besides, by employing functionalized organic linkers, the light-responsive range of MOFs can be extended. Recently, more and more efforts have been devoted to integrating metal nanoparticles and inorganic semiconductor into the 3-D framework of MOFs[30-33] and implementing the molecular engineering by utilizing the photoactive organic ligands[34-37], aiming to improve the optical, photoelectric, electrochemical, and photocatalytic properties of MOFs[33, 34, 37-39] In the meantime, a few reports involved the MOFs/graphene hybrids with functionalized graphene as a building block for oxygen reduction and solar-to-chemical energy conversion, and showed that the incorporation of graphene can improve the electrocatalytic and photocatalytic properties of semiconducting MOFs.[38, 40, 41] In most cases, graphene or GO nanosheets severed as synthetic supports for the surface decoration or encapsulation of dispersed MOF nanocrystals.[40-43] The interconnection of graphene with photoactive MOFs to form the sandwich nanoarchitectures, which may exert the

State Key Laboratory of Photocatalysis on Energy and Environment, School of Chemistry, Fuzhou University, Fuzhou 350116, People's Republic of China, Email: jllong@fzu.edu.cn (J. Long)

Electronic Supplementary Information (ESI) available: Including the XRD patterns, SEM images and TEM images of the parent NH_2-MIL-125(Ti) and graphene/NH_2-MIL-125(Ti) composite, the ^{1}HNMR spectra of pyrene$^+$ and pyrene$^+$-GO, the XRD patterns and SEM images and photocatalytic test results of the reference samples, the Raman spectra and FT-IR spectra of xrGO/UiO-66-NH_2 hybrids, and UV-vis absorption and FT-IR spectra of pyrene$^+$, TGA pattern; all of the above, see DOI: 10.1039/x0xx00000x

efficient separation and transfer of charges in the established electron donor-acceptor conjugates, nevertheless has been rare. To this end, it is intriguing to explore the integration of graphene with MOFs, which leads to the hierarchical architecture, and the potential applications of the intelligent hybrid in electronics, photovoltaic devices, or solar energy conversion.

Herein, we report the hierarchical nanoarchitectures composed of reduced graphene oxide (rGO, which is generally called graphene) and photoactive MOFs materials, where graphene and MOFs are separately utilized as a 2-D scaffold and the building blocks. The fabricated hybrid, xrGO/UiO-66-NH_2, with different graphene contents, were extensively characterized, focusing on the structural and physicochemical characteristics, photoresponse features, photocatalytic performance and electrochemical behaviors. The results indicate that the hierarchical sandwich nanoheterostructure is able to boost the selective photocatalytic oxidation of benyl alcohol, and induces a higher photocatalytic activity than the parent MOFs. Finally, according to the detailed analysis, a tentative mechanism was proposed to well explain the enhancement of organic photosynthesis. Furthermore, the strategy was also attested effective for the assembling of rGO with other NH_2 groups –containing MOFs, such as NH_2-MIL-125(Ti), implying its generality.

Experimental Section

Chemical reagents used for the preparation of samples and photocatalytic activity test, which include graphite powder, concentrated H_2SO_4, $NaNO_3$, $KMnO_4$, H_2O_2, HCl, N, N'-dimethylformamide (DMF), anhydrous methanol, benzylic alcohol and trichloromethane, are all of analytical grade purity without further purification prior to use. They were all purchased from Sinopharm Chemical Reagent Co., Ltd. Metal salts ($ZrCl_4$) (98%) and organic linkers (2-aminoterephthalic acid) (99%) used for the synthesis of UiO-66-NH_2 MOFs were bought from Aladdin Co., Ltd. and Alfa Co., Ltd. respectively. Reagents for the preparation of pyrene$^+$, which include anhydrous tetrahydrofuran (THF) (99.9%), trimethylamine (TMA) in THF (2 mmol/mL), 1-(bromoacetyl) pyrene (97%), and dimethyl Sulfoxide-d6 (DMSO-d6) were purchased respectively from Acros Organics Co., Ltd., TGI and J & K scientific Co., Ltd. Trifluoromethylbenzene (99%) used for the solvent of photocatalytic activity test and 4-bitrobenzyl alcohol (98%), 4-fluorobenzyl alcohol (98%) and 4-methylbenzyl alcohol (98%) were bought from Aladdin Co., Ltd. Acetonitrile of HPLC grade purity bought from Sinopharm Chemical Reagent Co., Ltd.

Preparation of Graphene Oxide

The modified Hummers method was used herein to synthesize graphene oxide. The specific procedure was referred to Liu's work.[62]

Preparation of Pyrene$^+$ (Trimethyl-(2-oxo-2-pyrene-1-yl-ethyl)-ammonium bromide)

Based on the method reported by Nakashima et al.,[47] the pyrene-carrying ammonium cation was prepared. It should be noted that differing from the use of the trimethylamine gas by Nakashima et al., we employed the THF dispersion of trimethylamine as the original source of trimethylamine. The ^{1}HNMR, UV-vis absorption and IR spectra shown in Figure S4, Figure S10 and 11 (see Supporting Information) confirm the successful synthesis.

Synthesis of UiO-66-NH_2

UiO-66-NH_2 MOFs was synthesized according to the method reported by Cavka et al.[44]

Synthesis of NH_2-MIL-125(Ti)

NH_2-MIL-125(Ti) was prepared adopting the method reported by Fu et al.[63] Specifically, 2-aminoterephthalic acid (H_2BDC-NH_2) (9 mmol) was added into the mixed solution of DMF (27 mL) and anhydrous methanol (3 mL), and then tetrabutyl titanate (2.25 mmol, 0.78 mL) was added, followed by stirring at ambient temperature for 30 min. The mixed solution was then transferred into a 100 mL autoclave and heated to 150 ℃ for 72 h. After the autoclave was cooled to the room temperature, the solid was filtered and immersed in anhydrous methanol for 4 days with stirring. The methanol was changed twice every day. The product was finally dries at 85 ℃ under vacuum for 12 h. The resulting solid was preserved in a desiccator for use.

Fabrication of rGO/UiO-66-NH_2

For fabrication of rGO/UiO-66-NH_2 hybrid, firstly, a certain volume of graphene oxide (GO) aqueous dispersion (1.6 mg/mL) was added to 150 mL of DMF, and the added weight of GO was according to the amount of MOFs synthesized with the same amount of precursors and solvent. After ultrasonication of 30 min, pyrene$^+$ was added into the mixture and its concentration was 0.25 mM, which is followed by ultrasonication for 30 min. And then part of ligand (2-aminoterephthalic acid (H_2BDC-NH_2), 1.362 mmol) was added and stirred overnight at ambient temperature. Then metal salts ($ZrCl_4$, 1.362 mmol) and another part of ligand (H_2BDC-NH_2, 1.362 mmol) were added into the mixed solution. After stirring for 30 min at room temperature, the final mixing solution was transferred to a 50 mL autoclave and heated to 120℃ for 48 h. The product was cooled to room temperature at ambient environment. The solid was filtered and immersed in anhydrous methanol for 5 days with stirring. The methanol was changed twice every day. Finally, the obtained solid was dried at 80 ℃ under vacuum for 10 h. The resulting solid was preserved in a desiccator for use.

The abovementioned fabrication procedure of rGO/UiO-66-NH_2 hybrid was applied to synthesize the 1.0rGO/UiO-66-NH_2-NP reference sample without the addition of pyrene$^+$. The 1.0rGO/UiO-66-NH_2-SL reference sample was prepared by a procedure without the pre-anchoring step of ligand on the graphene oxide (GO).

Fabrication of rGO/NH_2-MIL-125(Ti)

The functionalization procedure of graphene oxide with pyrene$^+$ and 2-aminoterephthalic acid (H_2BDC-NH_2) was the same as the fabrication of rGO/UiO-66-NH_2 except for the amount of 2-aminoterephthalic acid (9 mmol). The solvothermal reaction was the same as the synthesis of the

parent NH_2-MIL-125(Ti) except for the amount of tetrabutyl titanate (4.5 mmol, 1.56 mL).

Catalyst Characterizations

X-ray power diffraction data were recorded on a Bruker D8 Advance X-ray diffractometer equipped with a Cu Kα X-ray source (λ = 1.5406 Å). Data were collected at room temperature (296 K), from 5° to 40° at a step width of 0.01°. Scanning electron microscopy images of samples were taken with a Hitachi S-5800 system. Transmission electron microscopy images were collected on a JEOL model JEM 2010 EX microscope at an accelerating voltage of 200 KV. The nitrogen adsorption and desorption isotherms were determined on Micromeritics apparatus of model ASAP 2020 and by the Brunauer- Emmett-Teller (BET) method at 77 K. The X-ray photoelectron spectroscopy data were carried out on an ESCALAB 250 XPS system with a monochromatized Al Kα X-ray source (15 KV, 200 W, 500 μm, pass energy = 20 eV). The FTIR spectra of samples were recorded using a Nicolet Magna 670 FTIR spectrometer with a DTGS detector. The Raman spectra of samples were collected on in via-Reflex Micro-Raman Spectroscopy System 1000 with a laser excitation source of 532 nm. The UV-vis diffused reflectance spectra were measured on a Varian Cary 500 Scan UV/Vis system ranging from 200 to 800 nm. Nuclear magnetic resonance (NMR) was carried out on a Bruker AVANCE Ⅲ 500 system. The electrochemical analysis including transient photocurrent response and electrochemical impendence spectra were carried out on an epsilon workstation and a ZENNIUM workstation, respectively. The photocurrent test was conducted in $NaSO_4$ aqueous solution (0.2 M) and the electrochemical impedance spectroscopy (EIS) recording was performed in the electrolyte composed of KCl aqueous solution (0.5 M) and $K_3[Fe(CN)_6]/K_4[Fe(CN)_6]$ (0.01 M) with a ratio of 1:1.

The electrode was prepared as follows: firstly, 0.0046 g catalyst were dispersed in 0.5 mL alcohol to form suspension liquid by stirring for several hours, and then 10 uL of the suspension liquid was dropped on the FTO conducting glass to form a thin square layer of 5 mm × 5 mm, and finally other space, except for the square layer and the front space left for linking with the electrode, was insulated by printing a layer of enamel, ensuring that the current is completely originated from the light-excited catalyst.

Photocatalytic Activity Test

The photocatalytic activities test was conducted in a sealed 10 mL Pyrex glass reactor at ambient temperature. 0.025 g of photocatalyst, 0.5 mmol of benzyl alcohol and 2.5 mL of benzotrifluoride (BTF) saturated with molecular oxygen in advance were loaded into the reactor and then the whole system was sealed. Before irradiation with a 300 W Xe lamp with visible light of wavelength ≥ 420 nm, the system was stirred in the dark for onr hour with a magnetic stirrer (1000 rpm) to ensure the establishment of adsorption-desorption equilibrium between the catalyst and the substrate. After irradiation of 8 h, the suspension was centrifuged at 12000 rpm for 10 min and the supernatant was diluted to one fiftieth with acetonitrile, after the dilution was analyzed with high performance liquid chromatography (HPLC). As for aromatic alcohols of 4-nitrobenzyl alcohol, 4-fluorobenzyl alcohol and 4-methylbenzyl alcohol, their dispersions in BTF with a certain concentration, which had been saturated with molecular oxygen in advance, were added into the reactor to proceed to the photocatalytic activity test. The content of 4-nitrobenzyl alcohol was 0.05 mmol, because it is difficult to dissolve in BTF.

In the evaluation of the photocatalytic activities of these as-prepared samples, the conversion of alcohols and the selectivity to corresponding aldehydes were defined as follows respectively:

Conversion (%) = $[(C_0-C_{alcohol})/C_0] \times 100$

Selectivity (%) = $[C_{aldehyde}/(C_0-C_{alcohol})] \times 100$

where C_0 is the initial concentration of aromatic alcohol, $C_{alcohol}$ is the concentration of aldehyde synthesized from alcohol after irradiation of 8 h.

Results and Discussion

Visible-light responsive UiO-66-NH_2 MOF, an extension of Zr-based MOFs (UiO-66), has been on the focus since they were first reported by Cavka et al. in 2010,[44] for its visible light photoresponse and the structural feature and physicochemical properties similar to UiO-66. To realize the hierarchical sandwich nanoarchitecture by the integration of rGO with UiO-66-NH_2 MOFs, many impediments need to be surmounted, the main subject of which lies in how to ingeniously link the MOFs on the flat surface of rGO to form the intimate contact. Our investigation indicates that the simple straightforward solvothermal growth of UiO-66-NH_2 on graphene fails generally to form the nanoheterostructured hybrids because of the irreversibly restacking aggregation of graphene and the weak interaction force between GO and the constitutes of MOFs. Implementing aryl diazonium salt functionalization for rGO, which is one of the covalent functionalization methods for modifying rGO, and then connecting the functionalized rGO with MOFs via the anchored carboxyl ligands in the pre-processed diazonium salt procedure, which is the strategy employed in the work of Jahan[40, 42] and Kumar,[43] is relatively complicated and the functionalization degree is not easy to control, affecting the electric conductivity of the resulting product. Furthermore, the attachment of functional groups, which prefer to link to the edges of graphene, [45] may convert the carbon atoms of graphene from sp^2 to sp^3. It disrupts the π-network of graphene and hence decreases its electronic properties. In order to overcome the aforementioned disadvantages, an innovative strategy is employed herein for the fabrication of the layered rGO/UiO-66-NH_2 sandwich hybrids. As described in Scheme 1, we first functionalize graphene oxide (GO) with trimethyl-(2-oxo-2-pyren-1-yl-ethyl)-ammonium bromide (pyrene$^+$) in N,N-dimethylformamide (DMF), and then a small amount of 2-aminoterephthalate acid is anchored in advance to pyrene$^+$ by the electrostatic interaction, and finally a fixed amount of Zr^{4+} and 2-aminoterephthalate acid are added. Then by undergoing the solvothermal procedure of 48 h at 120 ℃, UiO-66-NH_2 MOFs

are formed and GO is partly reduced into rGO. At the same time, the procedure for the hybridization of MOFs with rGO also proceeds by the coordination between metal centre,

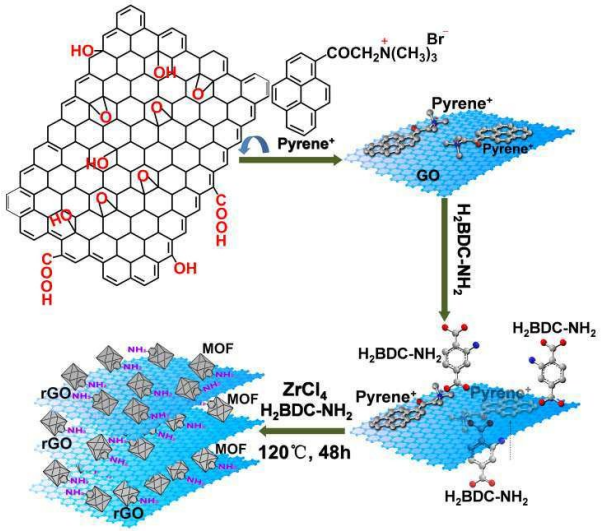

Scheme 1. Diagrammatic sketch of stepwise fabrication procedures for the layered rGO/UiO-66-NH_2 hybrids.

Zr^{4+}, and 2-aminoterephthalate acid pre-anchored to pyrene$^+$ and those post-added organic linkers. Herein, pyrene$^+$, an amphiphilic pyrene derivative, plays the pivotal role in the successful integration. Pyrene$^+$ has been already proven to be an excellent stabilizer and exfoliator for carbon nanotube,[46-48] and a connector between carbon nanotubes with other photo-active chromophores, such as porphyrin derivatives,[49,50] Considered that graphene itself is the primary unit for all of the carbon allotropes, many modification strategies applied for carbon nanotube are consequently testified on graphene, which can facilitate to fabrication of graphene-based conjugates. Dirian, Malig et al. has made extensive and profound studies on the integration of nanocarbons materials, including carbon nanotubes and functionalized graphene, with other various building blocks.[23, 50] As they classified, covalent and noncovalent modifications are two different rGO functionalization methods with respective advantages and disadvantages. Compared with the covalent functionalization which often suffers from the main drawback of disrupting the π-network, the noncovalent modification is better when assembled with other photo-active chromophores. Their work implied that pyrene$^+$ may be an effective mediator for the formation of electron donor-acceptor conjugates composed of graphene and building blocks, such as porphyrin$^-$, CdTe quantum dots (QDs), other sensitizers like subphthalocyanine, etc., via the π-π interactions and the electrostatic interaction.[23, 51, 52] In this work, it was used for the *in-situ* fabrication of hierarchical rGO/MOFs hybrids, and the most distinction lies in not only the building blocks, MOFs, but the demonstration of the enhanced photocatalytic performance over the layered assembly. By adopting the particular strategy, a series of the layered rGO/UiO-66-NH_2 sandwich hybrids with different rGO/UiO-66-NH_2 weight ratios (denoted as *x*rGO/UiO-66-NH_2, where *x* is the rGO content) were prepared to screen out an optimal photocatalyst. We also attempt to use the strategy to prepare the layered nanoarchitecture composed of NH_2-MIL-125(Ti) and graphene.

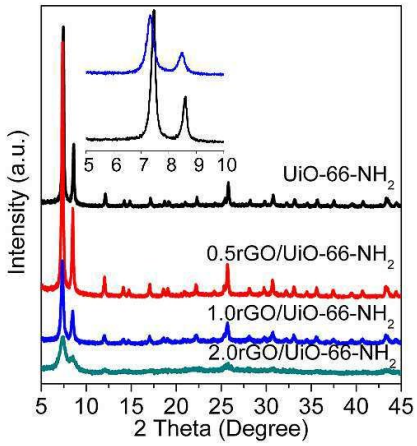

Figure 1. XRD patterns of as-prepared samples.

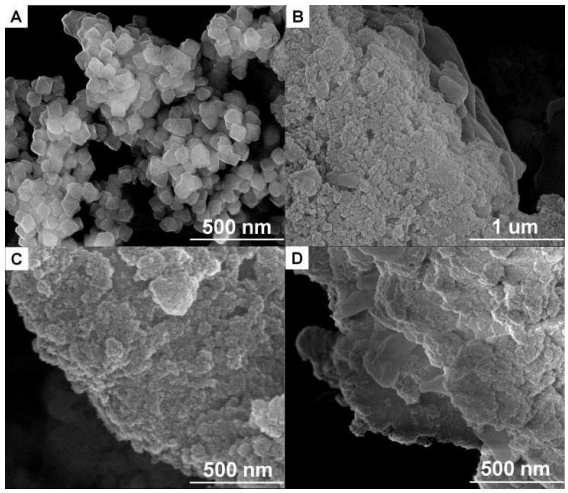

Figure 2. SEM images of UiO-66-NH2 (A), 0.5rGO/UiO-66-NH_2 (B), 1.0rGO/UiO-66-NH_2 (C), and 2.0rGO/UiO-66-NH_2 (D).

The structure and morphology of the final products, rGO/UiO-66-NH_2 hybrids, were investigated first by X-ray diffraction. As displayed in Figure 1, all of the as-synthesized hybrids exhibit the characteristic diffraction peaks of UiO-66-NH_2, indicating the successful growth and formation of UiO-66-NH_2 on rGO. Attention should be paid that at 2.0 wt% of graphene content, the characteristic diffraction features of UiO-66-NH_2, especially the two diffraction peaks at 5-10 degrees, are greatly broadened and decreased in intensity. This is highly consistent with the result reported by Schaate et al.[53] who have demonstrated that the existence and percentage of water can severely influence both the

crystallinity and particle size of UiO-66-NH_2, and particularly a small amount of water can impair the crystallinity of MOFs, as the 0.5rGO/UiO-66-NH_2 sample disclosed. Importantly, we found all diffraction peaks of the rGO/UiO-66-NH_2 hybrids visibly shifted toward low angle compared with those of pure UiO-66-NH_2 sample. This indicates the occurrence of the strong interaction between graphene and UiO-66-NH_2 in the rGO/UiO-66-NH_2hybrids.

Figure 2 shows the SEM images of all as-synthesized samples. The parent UiO-66-NH_2 (Figure 2A) crystallizes as homogeneous inter-grown cubic crystals as reported by Cavka and Long.[34,44] The pure UiO-66-NH_2 particles are dispersed and accumulated in a random way, whereas the rGO/UiO-66-NH_2 hybrids pack layer-by-layer in a regular way (Figure 2B-D). It can be clearly seen that rGO severs as a 2-D flat platform supporting the formation and growth of UiO-66-NH_2 layers. The sandwich-like heterostructure formed by the orderly stacking of rGO and UiO-66-NH_2 is clearly discernible for the three hybrids, 0.5rGO/UiO-66-NH_2, 1.0rGO/UiO-66-NH_2, and 2.0rGO/UiO-66-NH_2. The SEM images shown in Figure S2 (See Supporting Information) also display the clear formation of the layered rGO/NH_2-MIL-125(Ti) nanoarchitecture. Hence, the synthesis strategy has a considerable generality for other MOFs materials.

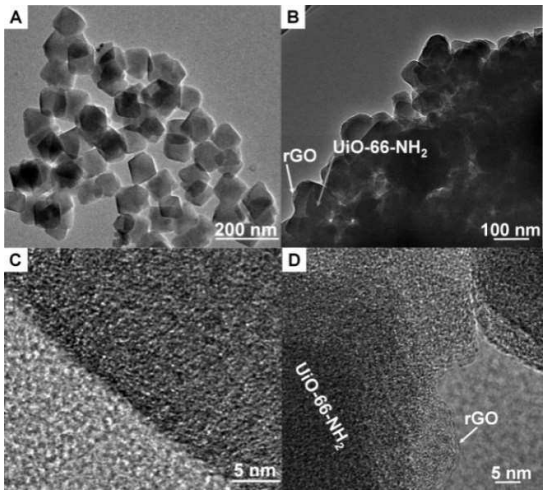

Figure 3. TEM and HRTEM images of UiO-66-NH_2 (A, C) and 1.0rGO/UiO-66-NH_2 (B, D).

Figure 3 illuminates the TEM and HRTEM images of UiO-66-NH_2 and 1.0rGO/UiO-66-NH_2. The TEM and HRTEM images of NH_2-MIL-125(Ti) and rGO/NH_2-MIL-125(Ti) hybrid are displayed in Figure S3 (see Supporting Information). No lattice fringes are observed in the HRTEM images of pure UiO-66-NH_2 (Figure 3B) and NH_2-MIL-125(Ti) (Figure S3B, see Supporting Information), whereas the clear-cut outline of MOF nanoparticles is clearly discerned. For the 1.0rGO/UiO-66-NH_2 hybrid, we have to observe the boundary of the assembly because electrons do not penetrate in the centre, as shown in Figure 3D and S3D (see Supporting Information). The wrinkles of rGO sheets are clearly discernible at the margin of the hybrid nanoarchitecture, further confirming the formation of layered hetero-nanostructures by orderly stacking of rGO and UiO-66-NH_2 nanoparticles via the pyrene$^+$ linker.

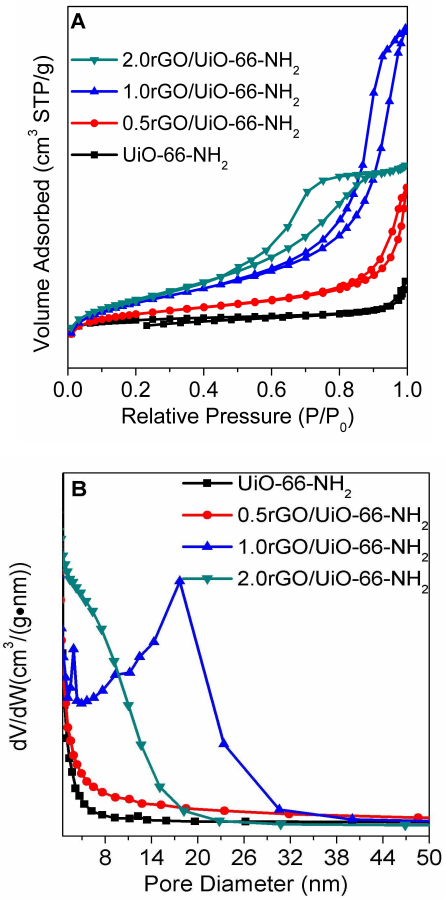

Figure 4. Nitrogen adsorption-desorption isotherms curve (A) and pore size distribution plots (B).

More obvious evidence to illustrate the feasibility of the strategy we employed here, was obtained by ^{1}HNMR spectral measurement. As displayed in Figure S4, the chemical shift values of protons in pyrene$^+$-GO shifted to higher magnetic field compared with pyrene$^+$, which apparently indicates the existence of noncovalent π-π interactions between GO, which is the precursor of rGO, and amphiphilic pyrene$^+$.[47] The interaction provides more possibilities for anchoring of organic linkers of MOFs on the GO surface, and is helpful to prevent rGO from aggregating during the solvothermal reduction of part of GO to rGO. Moreover, attention should be paid to a distinctive difference of the particle size between the pure UiO-66-NH_2 and the rGO/UiO-66-NH_2 hybrids. The former has a particle size of ca. 90 nm (Figure 2A and 3A), far larger than the latter (Figure 2B, 2C and 2D), but just slightly larger than the sample synthesized with double content of ligand (UiO-66-NH_2-DL, Figure S6B), and comparable to the 1.0rGO/UiO-66-NH_2 counterpart synthesized without adding pyrene$^+$ (1.0rGO/UiO-66-NH_2-NP, Figure S6C). By observing the

prepared counterparts, UiO-66-NH_2-DL (Figure S6B), 1.0rGO/UiO-66-NH_2-NP (without pyrene$^+$, Figure S6C) and also the 1.0rGO/UiO-66-NH_2-SL (without pre-anchoring ligands on rGO, Figure S6D), we can make the conclusion that both the ligand amount and pyrene$^+$ affect the particle size, especially the latter, which functions as an effective linker for rGO and MOFs and influences the growth of MOFs on rGO. The decreased particle size and the intimate contact between the UiO-66-NH_2 layer and the rGO layer can facilitate the transfer of photogenerated electrons from the UiO-66-NH_2 moieties to the rGO moieties, consequently enhancing the photocatalytic activity.

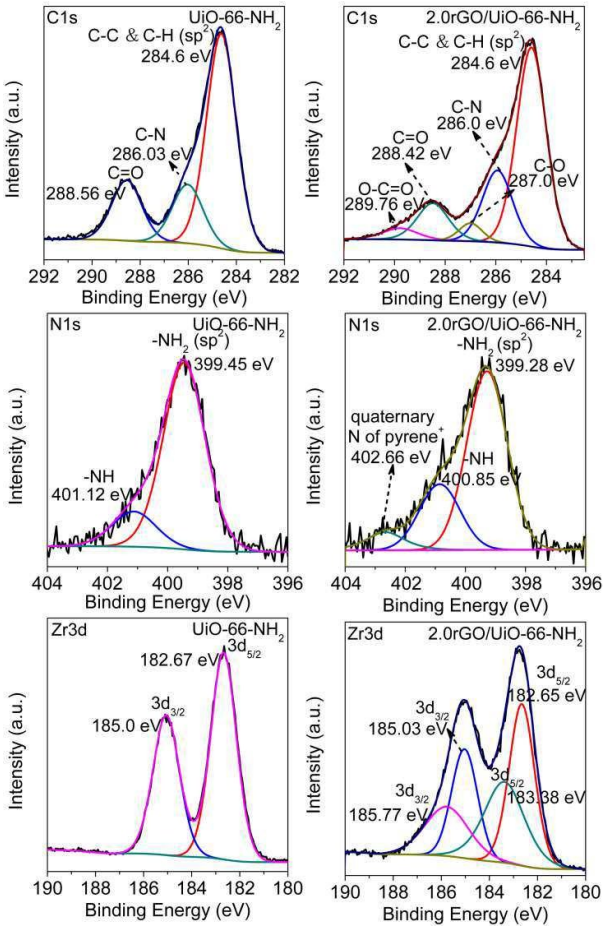

Figure 5. C1s, Zr3d, and N1s XPS Spectra of UiO-66-NH_2 and 2.0rGO/ UiO-66-NH_2.

The textural properties of the rGO/UiO-66-NH_2 hybrids with different rGO percentages were investigated by nitrogen adsorption-desorption at 77 K. As shown in Figure 4A, the pure UiO-66-NH_2 possesses the typical type I of adsorption isotherm shape corresponding to zeolite and zeolite-like crystalline solids according to the IUPAC classification,[54] and has a Langmuir surface area of ca. 800 $m^2 g^{-1}$. This clearly indicates the microporous properties. With the addition of rGO, the hybrids present the typical type IV of adsorption isotherm shape, whereas the Langmuir surface area of ca. 750 $\pm$ 20 $m^2 g^{-1}$ is comparable to the pure UiO-66-NH_2. The 0.5rGO/UiO-66-NH_2 and 1.0rGO/UiO-66-NH_2 hybrids give a type H1 hysteresis loop, while the 2.0rGO/UiO-66-NH_2 hybrid shows a type H_2 hysteresis loop with ink-bottle shaped pores (pore body larger than pore mouth). It can be seen from Figure 4B that the 0.5 rGO/UiO-66-NH_2 and 2.0rGO/UiO-66-NH_2 hybrids do not show the mesopore size distribution plots calculated by BJH method. Exceptionally, the pore size of the 1.0rGO/UiO-66-NH_2 hybrid is distributed at range of 7-32 nm, possibly due to the orderly stacking of UiO-66-NH_2 nanoparticles between graphene layers. The mesoporous properties are considerably beneficial for the transport of reactive substrates into active sites.

Fourier transform infrared (FTIR) and Raman spectroscopies were applied to further characterize the hybrids, as shown in the Supporting Information, Figure S7 and S8, all of the IR vibration bands for the 1.0rGO/UiO-66-NH_2 hybrid are fully consistent with those of the parent UiO-66-NH_2, further suggesting the hybrids have the same chemical structure as the parent UiO-66-NH_2. Comparison of Raman spectra of the *x*rGO/UiO-66-NH_2 hybrids and GO finds that both of the D band at ca. 1310 cm^{-1} belonging to the disorder-induced vibrational mode and the G band at ca. 1600 cm^{-1} representing the E_{2g} vibration mode of the sp^2-bonded graphitic carbons are relatively changed in intensity after the solvothermal process. The intensity ratio of the latter to the former (the I_G/I_D ratio), which is an indicative of the degree of structural defects and a quantitative measurement of edge plane exposure,[55] for the rGO/UiO-66-NH_2 hybrids is lower than that of GO. This suggests that the GO filled into UiO-66-NH_2 are partly reduced into graphene by the solvothermal treatment under the synthesis conditions.

XPS was used to further study the chemical states of C, N and Zr in the hybrids (Figure 5). As indicated by the C1s core level XPS spectra, the pure UiO-66-NH_2 nanocrystals show two peaks at 288.56 and 286.03 eV, which belong to the O-C=O and C-N groups of the NH_2-BDC_2^- linker, respectively, whereas the 2.0rGO/UiO-66-NH_2 hybrid gives two sets of C1s XPS peaks, i.e., the three features attributed to GO and/or rGO at 289.76, 287.0, and 284.6 eV and the set of peaks ascribed to the organic linker of UiO-66-NH_2 occurring at 288.42 and 285.89 eV, which shifted by 0.14 eV toward low energy. The result is believed to be the indication of the following two aspects: (1) the successful integration of rGO with UiO-66-NH_2; (2) the electron density around the organic linkers is increased greatly by the insertion of graphene layers. This can be further confirmed by N1s XPS spectra. It can be seen clearly that the two N1s peaks at 399.45 and 401.12 eV corresponding to the –NH_2 and –NH groups of the organic linkers in pure UiO-66-NH_2 nanocrystals are shifted to 399.28 and 400.85 eV, respectively, after the hybridization with rGO. It is noteworthy that a weak N1s peak occurs at 402.66 eV. It is attributable to the quaternary N of pyrene$^+$,[56] suggesting the successful π-stacking of pyrene$^+$ on graphene. Interestingly, comparison of the Zr3d XPS spectra finds that a set of new binding energies at 185.77 and 183.38 eV, besides the set of peaks at 185.03 and 182.65 eV, is discernible for the 2.0rGO/UiO-66-NH_2 hybrid, as a result of the filled graphene sheets. The significant shift (Δ= +0.74 eV)

of the Zr3d binding energies toward high energy indicates the strong electron-drawing effect of the rGO layers for the metal component. Taking both the electron-drawing effect of rGO for metal and the electron-depositing effect for organic linker into account, it can be concluded that the filler, rGO introduced in a regular way, alters the electronic properties of the UiO-66-NH_2 nanocrystals by the noncovalent linker, pyrene$^+$, between rGO and MOFs.

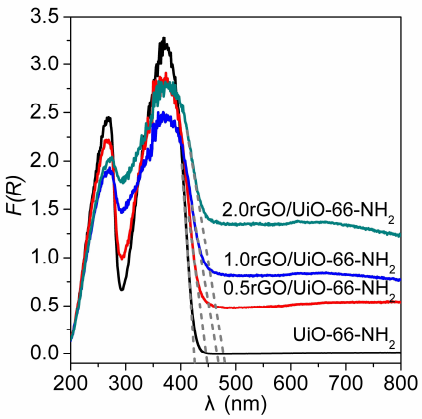

Figure 6. UV-vis diffused reflectance spectra of UiO-66-NH_2 and *x*rGO/UiO-66-NH_2.

UV-vis diffuse reflectance spectroscopy was applied to study how the layered heterostructure influence the optical properties of UiO-66-NH_2 nanocrystals. As shown in Figure 6, UiO-66-NH_2 has two absorptions in the region of 200-800 nm with an absorption band edge of ca. 430 nm, corresponding to the band gap energy of 2.88 eV. After adding graphene, the absorption at the range of 400-800 nm is significantly intensified with increasing graphene content, which is the same as that observed in the rGO/TiO_2[57] and rGO/CdS[58] as well as other rGO-based inorganic semiconductor hybrids,[10,59] and the red-shift of the absorption edge for the *x*rGO/UiO-66-NH_2 hybrids (*x* = 0.5, 1.0, 2.0) is clearly discernible. Furthermore, the red-shift increases with increasing graphene contents. This clearly indicates the enhancement of solar energy utilization, as a result of the particular sandwich-like heterostructure benefited from the close contact between UiO-66-NH_2 and rGO.

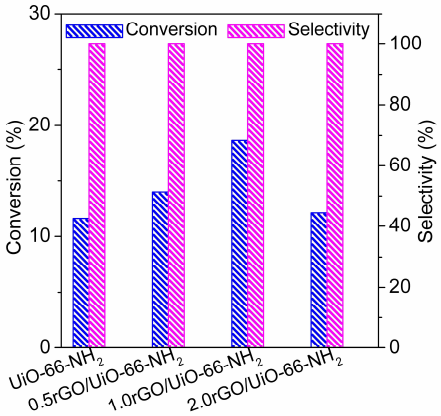

Figure 7. Photocatalytic activity of UiO-66-NH_2 and *x*rGO/UiO-66-NH_2.

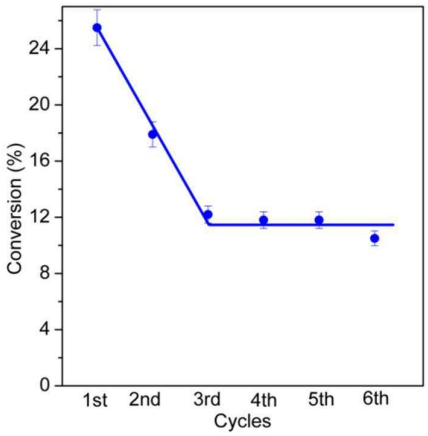

Figure 8. Photocatalytic activity stability of 1.0rGO/UiO-66-NH_2 (B) (Reaction conditions: benzyl alcohol (0.5 mmol), photocatalysts (0.025 g), solvent of benzotrifluoride (BTF) (2.5 mL), irradiation wavelength (λ > 420 nm), irradiation time (8 h), irradiation intensity (660 mW)).

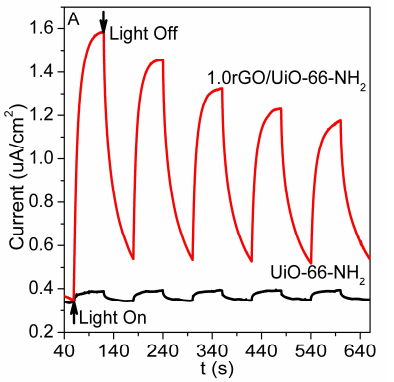

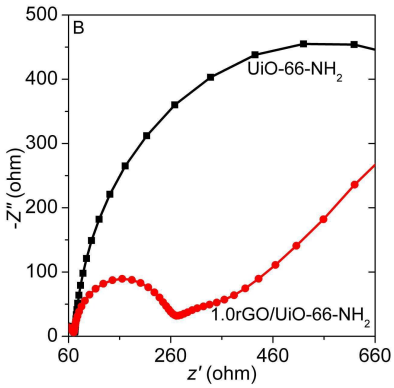

Figure 9. Photocurrent responses of the pure UiO-66-NH_2 and 1.0rGO/ UiO-66-NH_2 (A). Electrochemical impedance spectroscopy (EIS) Nyquist diagrams of the pure UiO-66-NH_2 and 1.0rGO/ UiO-66-NH_2 (B) in the electrolyte composed of KCl

aqueous solution (0.5 M) and $K_3[Fe(CN)_6]/K_4[Fe(CN)_6]$ (0.01 M) with a ratio of 1:1.

The photocatalytic properties of the sandwich-like hybrids were evaluated by applying the liquid-phase selective aerobic oxidation of aromatic alcohols as a model reaction under visible light (λ ≥ 420 nm) at ambient temperature. The result was displayed in Figure 7. All of the layered hybrids with different graphene weight ratios present the enhanced photocatalytic conversion in comparison to the pure UiO-66-NH_2, suggesting that the insertion of graphene is beneficial for improving the photocatalytic performance of UiO-66-NH_2. The photocatalytic conversion of benzylic alcohol increases with increasing rGO content and reaches a maximum at 1.0 wt% of rGO, where a conversion of 18.6% is achieved within 8 h of illumination. However, when the graphene content is more than 1.0 wt%, the conversion decreases sharply, implying the negative effect of the excessive graphene on the photocatalytic performance. This is mainly because the excessive rGO shields the UiO-66-NH_2 MOFs from absorbing visible light and consequently reduce the concentration of photogenerated charges.[57-60] Notably, a quantum yield (QY) value of ca. 2.1% is achieved over the 1.0rGO/UiO-66-NH_2 hybrid under 400 nm light irradiation.

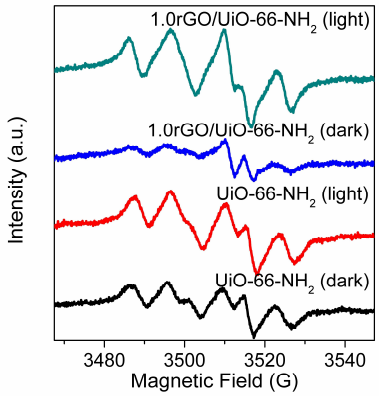

Figure 10. DMPO-trapped EPR spectra of UiO-66-NH_2 and 1.0rGO/ UiO-66-NH_2 dispersed in methanol.

Figure 8 illuminates a typical curve of the activity stability of the 1.0rGO/UiO-66-NH_2 hybrid. It appears that the activity initially decreases. This is mainly due to the severe blocking of MOF pore structures. However, after 3 times of cyclic use, the hybrid gives a stable photocatalytic conversion at ca. 12.0% for benzylic alcohol, which is still higher than that (ca. 6.0%) of pure UiO-66-NH_2 following the action curve similar to the hybrid. The enhanced conversion further indicates the impressive function of the rGO layers inserted in the sandwich-like nanoarchitecture as an electron transfer mediator.

4-Nitrobenzyl alcohol, 4-methylbenzyl alcohol, and 4-fluorobenzyl alcohol were chosen to testify the wide applicability of the rGO/UiO-66-NH_2 hybrids (Table 1). It appears that the optimal hybrid, 1.0rGO/UiO-66-NH_2, is capable to multiply the conversion of UiO-66-NH_2 for these photo-oxidation reactions when the -R group is –F and –NO_2. Based on the characterizations above, it is reasonable to propose that the improved photoactivity might be contributed mainly from the unique sandwich-like heterostructure, which can ensure the intimate contact between rGO and UiO-66-NH_2 and hence ensure the acceleration of the photogenerated electron transfer from the UiO-66-NH_2 to rGO. Furthermore, for the four reactions, 100% selectivity is achieved, suggesting the application potential of the hybrid materials in organic photosynthesis. Interestingly, the conversion is closely related to the electron-drawing capability of the -R group, which decreases in the order of –NO_2 (43.1%) > -F (33.0%) > -H (17.7%) > -CH_3 (16.3%). The activity result is reverse to that of the $C_3N_3S_3$ polymer/graphene hybrid[10], implying the mechanistic difference.

To further verify the contribution of the layered "sandwich" heterostructure to the enhanced photocatalytic conversion, we synthesized two counterparts with a 1.0 wt % content of rGO by varying the preparation procedure (denoted as 1.0rGO/UiO-66-NH_2-NP and –SL, respectively) and one parent MOF prepared with double content of organic ligand (UiO-66-NH_2-DL). The conversion of ca. 5% for UiO-66-NH_2-DL lower than that of UiO-66-NH_2 first excludes the contribution of the excessive organic ligand to the improved photocatalytic performance. The 1.0rGO/UiO-66-NH_2-NP hybrid prepared by the procedure without adding pyrene$^+$ shows a conversion of benzylic alcohol as low as ca. 5.0% (Figure S9, see Supporting Information), which is greatly lower than that of the 1.0rGO/UiO-66-NH_2 hybrid. The SEM image of the 1.0rGO/UiO-66-NH_2-NP hybrid (Figure S6C, See Supporting Information) displays irregular stacking of UiO-66-NH_2 nanocrystals on the rGO surface. Two conclusions can be drawn from these results: (1) the addition of pyrene$^+$ is indispensible for the self-assembly of rGO and MOFs to form the layered sandwich-like heterostructure; (2) the sandwich-like heterostructure can boost the photocatalytic conversion of benzylic alcohol. Such conclusions can be corroborated by the activity result of the 1.0rGO/UiO-66-NH_2-SL hybrid prepared by the one-spot solvothermal procedure (only adding the ligand, without prior anchoring of which to the pyrene$^+$), which gives a lower conversion (14.5%) of benzylic alcohol as comparison to the 1.0rGO/UiO-66-NH_2 hybrid. At the same time, by observing the SEM image of the 1.0rGO/UiO-66-NH_2-SL hybrid (Figure S6D), it can be found that MOFs in the 1.0rGO/UiO-66-NH_2-SL hybrid are contacted with rGO, but the ordered sandwich-like heterostructure is not well formed. This clearly illuminstates the success of the employed strategy, noncovalent organic functionalization combined with *in-situ* self-assembling by virtue of interface interaction, for the fabrication of the unique layered MOF/graphene heterostructures.

Table 1. Photocatalytic Oxidation of Several Typical Aromatic Alcohols over the Pure UiO-66-NH_2 MOF and the 1.0rGO/UiO-66-NH_2 Hybrid.

R groups	Photocatalysts	Conversion (%)
H	UiO-66-NH_2	11.6
	1.0rGO/UiO-66-NH_2	18.6
NO_2[a]	UiO-66-NH_2	18.9
	1.0rGO/UiO-66-NH_2	43.1
CH_3	UiO-66-NH_2	2.0
	1.0rGO/UiO-66-NH_2	16.3
F	UiO-66-NH_2	8.4
	1.0rGO/UiO-66-NH_2	33.0

Reaction conditions: aromatic alcohols (0.5 mmol), photocatalysts (0.025 g), solvent of benzotrifluoride (BTF) (2.5 mL) saturated with molecular oxygen in advance, irradiation wavelength (λ > 420 nm), irradiation time (8 h), irradiation intensity (450 mW). [a] 4-nitrobenzyl alcohol (0.05 mmol), solvent of BTF (3.5 mL).

Electrochemical analysis was conducted to understand the enhanced photoactivity of these hybrids (Figure 9). The 1.0rGO/UiO-66-NH_2 hybrid gives a much higher photocurrent than the parent UiO-66-NH_2 under visible light illumination (Figure 9A), verifying that with the aid of graphene, photo-induced charges do get more efficient transfer and separation due to the superior carrier mobility of graphene. In the Nyquist plots measured under the certain conditions (Figure 9B), a smaller hemicycle at high frequency corresponding to the double-layer capacitance can be observed for the 1.0rGO/UiO-66-NH_2 hybrid, further indicating the more efficient transfer of photo-generated carriers as a result of the rGO insertion. Hence, it is reasonable to make the conclusion that the sandwich-like heterostructure of the as-prepared MOF/graphene hybrids affords plenty of "quick channels" for the transfer and separation of photo-generated charges, consequently improving the photocatalytic activity.

To gain further insight into the photocatalytic reaction mechanism, electron spin resonance (ESR) spectroscopy was performed by recording active oxygen species generated under visible light irradiation, in which DMPO (5, 5-dimethyl-pyrroline N-oxide) was used as the trapping agent. It can be seen from Figure 10 that both the parent UiO-66-NH_2 and 1.0rGO/UiO-66-NH_2 hybrid already show one set of ESR signals in the dark, which corresponds to $\bullet O_2^-$ species formed in the micropores of UiO-66-NH_2 nanocrystals,[34] suggesting that oxygen can be activated by UiO-66-NH_2 nanocrystals. However, MOFs show no activity for the selective oxidation of benzylic alcohols in the dark, indicating the $\bullet O_2^-$ species are not the initiator to the photocatalytic reactions. Under visible light irradiation, the ESR signals of $\bullet O_2^-$ species are intensified significantly for the 1.0rGO/UiO-66-NH_2 hybrid, whereas the pure UiO-66-NH_2 shows a slight increase in intensity. The $\bullet O_2^-$ species of 1.0rGO/UiO-66-NH_2 sample visibly more than the parent UiO-66-NH_2 sample, which reflect the improved utilization of photo and photogenerated charges, as well as the more effective activation of surface-absorbed oxygen molecules, further confirming the conclusion that the filled graphene can accelerate the separation and transfer of photogenerated charges in the UiO-66-NH_2 moieties. No ESR signals of DMPO-•OH adduct species can be observed in water under visible light irradiation, indicating that water cannot be oxidized into •OH by the holes of UiO-66-NH_2 photocatalyst. The observation is highly consistent with the results reported by Long and Shen[34, 61]. Based on all characterizations and analysis above, we can thus propose that the activity improvement over the rGO/UiO-66-NH_2 hybrids follows a mechanism initiated by the hole-oxidization during the organic transformation (Scheme 2). Upon excitation with visible light, electrons and holes are generated in the UiO-66-NH_2 framework and then electrons are quickly transferred on the graphene layer. The molecular oxygen absorbed on graphene is reduced by electrons into $\bullet O_2^-$ species. Meanwhile, the aromatic alcohol substrates are oxidized to positive radical ions by deprotonation, which may be the rate-determining step of the aerobic oxidation. Finally, the positive carbonium ions of aromatic alcohols react with $\bullet O_2^-$ species to produce the corresponding aromatic aldehydes.

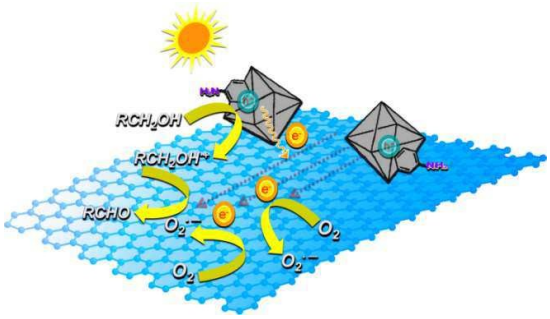

Scheme 2. Proposed mechanism for the enhanced photocatalytic oxidation over the fabricated hybrids.

Conclusions

In summary, by following the strategy of noncovalent methodology for graphene functionalization, in combination with *in-situ* self-assembling and solvothermal synthesis technique, we have successfully fabricated the layered MOFs/graphene hybrids, in which MOFs are immobilized on the flatland of graphene and vice versa graphene fills into MOFs building blocks, and demonstrated the enhanced photocatalytic performance for aromatic chemicals synthesis. The activity enhancement chiefly benefits from the unique sandwich-like heterostructure, which is able to boost the separation and transfer of photogenerated charges because of the intimate contact between rGO and MOFs by virtue of

pyrene+. This study not only affords an attractive and facile method for the preparation of photo-active MOFs/graphene hierarchical hybrids, but shows the application perspective of the layered sandwich-structure in solar-to chemical energy conversion. More comprehensive and extensive studies pertinent to design of the layered hybrids composed of photo-active building blocks and graphene are ongoing. In-depth study on the charge transfer behavior is envisioned to be of primary importance for the application of the hierarchical nanoarchitecture in graphene-based electronic, photovoltaic device and photocatalytic systems.

Acknowledgements

This work was financially supported by the NSFC (Grant Nos. 21003021, 21373051, and U1305242), the program for New Century Excellent Talents in Fujian Province University (JA14029), and the program for Qishan Scholar of Fuzhou University.

Notes and references

The authors declare no competing financial interest.

1. M. Chhowalla, H. S. Shin, G. Eda, L.-J. Li, K. P. Loh and H. Zhang, *Nat Chem*, 2013, **5**, 263-275.
2. X. Guo, Y. Wang, F. Wu, Y. Ni and S. Kokot, *Analyst*, 2015, **140**, 1119-1126.
3. X. Huang, Z. Zeng and H. Zhang, *Chem Soc Rev*, 2013, **42**, 1934-1946.
4. D. Voiry, M. Salehi, R. Silva, T. Fujita, M. Chen, T. Asefa, V. B. Shenoy, G. Eda and M. Chhowalla, *Nano Lett*, 2013, **13**, 6222-6227.
5. P. Norby, S. Johnsen and B. B. Iversen, *Phys Chem Chem Phys*, 2015, **17**, 9282-9287.
6. W. J. Ong, J. J. Yeong, L. L. Tan, B. T. Goh, S. T. Yong and S. P. Chai, *RSC Adv*, 2014, **4**, 59676-59685.
7. W. J. Ong, S. Y. Voon, L. L. Tan, B. T. Goh, S. T. Yong and S. P. Chai, *Ind Eng Chem Res*, 2014, **53**, 17333-17344.
8. Q. Han, F. Zhao, C. Hu, L. Lv, Z. Zhang, N. Chen and L. Qu, *Nano Research*, 2015, **8**, 1718-1728.
9. H. Zhang, Y. Wang, P. Liu, Y. Li, H. Yang, T. An, P. Wong, D. Wang, Z. Tang and H. Zhao, *Nano Energy*, 2015, **13**, 124-130.
10. J. Bian, Q. Li, C. Huang, J. Li, Y. Guo, M. Zaw and R.-Q. Zhang, *Nano Energy*, 2015, **15**, 353-361.
11. W. J. Ong, L. K. Putri, L. L. Tan, S.P. Chai and S. T. Yong, *Appl Cata B: Environmental*, 2016, **180**, 530-543.
12. K. Novoselov, *Nat Mater*, 2007, **6**, 720-721.
13. S. Stankovich, D. A. Dikin, G. H. B. Dommett, K. M. Kohlhaas, E. J. Zimney, E. A. Stach, R. D. Piner, S. T. Nguyen and R. S. Ruoff, *Nature*, 2006, **442**, 282-286.
14. R. Raccichini, A. Varzi, S. Passerini and B. Scrosati, *Nat Mater*, 2015, **14**, 271-279.
15. J. Long, X. Xie, J. Xu, Q. Gu, L. Chen and X. Wang, *ACS Catal*, 2012, **2**, 622-631.
16. J. Xu, L. Luo, G. Xiao, Z. Zhang, H. Lin, X. Wang and J. Long, *ACS Catal*, 2014, **4**, 3302-3306.
17. F. Bonaccorso, L. Colombo, G. Yu, M. Stoller, V. Tozzini, A. C. Ferrari, R. S. Ruoff and V. Pellegrini, *Science*, 2015, **347**.
18. Q. Xiang, J. Yu and M. Jaroniec, *J Am Chem Soc*, 2012, **134**, 6575-6578.
19. X. Huang, Z. Yin, S. Wu, X. Qi, Q. He, Q. Zhang, Q. Yan, F. Boey and H. Zhang, *Small*, 2011, **7**, 1876-1902.
20. Q. Xiang, B. Cheng and J. Yu, *Angew Chem Int Ed*, 2015, DOI: 10.1002/anie.201411096, n/a-n/a.
21. RamanathanT, A. A. Abdala, StankovichS, D. A. Dikin, M. Herrera Alonso, R. D. Piner, D. H. Adamson, H. C. Schniepp, ChenX, R. S. Ruoff, S. T. Nguyen, I. A. Aksay, R. K. Prud'Homme and L. C. Brinson, *Nat Nano*, 2008, **3**, 327-331.
22. J. Malig, N. Jux, D. Kiessling, J.-J. Cid, P. Vázquez, T. Torres and D. M. Guldi, *Angew Chem Int Ed*, 2011, **50**, 3561-3565.
23. J. Malig, N. Jux and D. M. Guldi, *Accounts Chem Res*, 2013, **46**, 53-64.
24. Q.-L. Zhu and Q. Xu, *Chem Soc Rev*, 2014, **43**, 5468-5512.
25. K. Zagorodniy, G. Seifert and H. Hermann, *Appl Phys Lett*, 2010, **97**, 1905.
26. U. Mueller, M. Schubert, F. Teich, H. Puetter, K. Schierle-Arndt and J. Pastre, *J Mater Chem*, 2006, **16**, 626-636.
27. L. E. Kreno, K. Leong, O. K. Farha, M. Allendorf, R. P. Van Duyne and J. T. Hupp, *Chem Rev*, 2011, **112**, 1105-1125.
28. P. Horcajada, T. Chalati, C. Serre, B. Gillet, C. Sebrie, T. Baati, J. F. Eubank, D. Heurtaux, P. Clayette, C. Kreuz, J.-S. Chang, Y. K. Hwang, V. Marsaud, P.-N. Bories, L. Cynober, S. Gil, G. Ferey, P. Couvreur and R. Gref, *Nat Mater*, 2010, **9**, 172-178.
29. T. Faust, *Nat Chem*, 2015, **7**, 270-271.
30. L. B. Vilhelmsen and D. S. Sholl, *The Journal of Physical Chemistry Letters*, 2012, **3**, 3702-3706.
31. J. Juan-Alcaniz, J. Gascon and F. Kapteijn, *J Mater Chem*, 2012, **22**, 10102-10118.
32. A. Dhakshinamoorthy and H. Garcia, *Chem Soc Rev*, 2012, **41**, 5262-5284.
33. T. Zhou, Y. Du, A. Borgna, J. Hong, Y. Wang, J. Han, W. Zhang and R. Xu, *Energy Environ Sci*, 2013, **6**, 3229-3234.
34. J. Long, S. Wang, Z. Ding, S. Wang, Y. Zhou, L. Huang and X. Wang, *Chem Commun*, 2012, **48**, 11656-11658.
35. G. E. Cmarik, M. Kim, S. M. Cohen and K. S. Walton, *Langmuir*, 2012, **28**, 15606-15613.
36. M. Kandiah, M. H. Nilsen, S. Usseglio, S. Jakobsen, U. Olsbye, M. Tilset, C. Larabi, E. A. Quadrelli, F. Bonino and K. P. Lillerud, *Chem Mater*, 2010, **22**, 6632-6640.
37. M. Kandiah, S. Usseglio, S. Svelle, U. Olsbye, K. P. Lillerud and M. Tilset, *J Mater Chem*, 2010, **20**, 9848-9851.
38. R. Lin, L. Shen, Z. Ren, W. Wu, Y. Tan, H. Fu, J. Zhang and L. Wu, *Chem Commun*, 2014, **50**, 8533-8535.
39. A. V. Vinogradov, H. Zaake-Hertling, E. Hey-Hawkins, A. V. Agafonov, G. Seisenbaeva, V. Kessler and V. V. Vinogradov, *Chem Commun*, 2014, **50**, 10210-10213.
40. M. Jahan, Q. Bao and K. P. Loh, *J Am Chem Soc*, 2012, **134**, 6707-6713.
41. L. Shen, L. Huang, S. Liang, R. Liang, N. Qin and L. Wu, *RSC Advances*, 2014, **4**, 2546-2549.
42. M. Jahan, Q. Bao, J.-X. Yang and K. P. Loh, *J Am Chem Soc*, 2010, **132**, 14487-14495.
43. R. Kumar, K. Jayaramulu, T. K. Maji and C. N. Rao, *Dalton Trans*, 2014, **43**, 7383-7386.
44. J. H. Cavka, S. Jakobsen, U. Olsbye, N. Guillou, C. Lamberti, S. Bordiga and K. P. Lillerud, *J Am Chem Soc*, 2008, **130**, 13850-13851.

45. R. Sharma, J. H. Baik, C. J. Perera and M. S. Strano, *Nano Lett*, 2010, **10**, 398-405.
46. Y. Tomonari, H. Murakami and N. Nakashima, *Chemistry-A European Journal*, 2006, **12**, 4027-4034.
47. N. Nakashima, Y. Tomonari and H. Murakami, *Chem Lett*, 2002, 638-639.
48. N. Nakashima, Y. Tanaka, Y. Tomonari, H. Murakami, H. Kataura, T. Sakaue and K. Yoshikawa, *J Phys Chem B*, 2005, **109**, 13076-13082.
49. C. Ehli, G. A. Rahman, N. Jux, D. Balbinot, D. M. Guldi, F. Paolucci, M. Marcaccio, D. Paolucci, M. Melle-Franco and F. Zerbetto, *J Am Chem Soc*, 2006, **128**, 11222-11231.
50. M. A. H. Konstantin Dirian, Georgios Katsukis, Jenny Malig, Laura Rodr´ıguez-P´erez, Carlos Romero-Nieto, Volker Strauss, Nazario Mart´ın, Dirk M. Guldi, *Chem. Sci.*, 2013, **4**, 4335-4353.
51. J. Malig, C. Romero-Nieto, N. Jux and D. M. Guldi, *Adv Mater*, 2012, **24**, 800-805.
52. C. B. Kc, G. N. Lim and F. D'Souza, *Angew Chem Int Ed Engl*, 2015, **54**, 5088-5092.
53. A. Schaate, P. Roy, A. Godt, J. Lippke, F. Waltz, M. Wiebcke and P. Behrens, *Chemistry-A European Journal*, 2011, **17**, 6643-6651.
54. G. Leofanti, M. Padovan, G. Tozzola and B. Venturelli, *Catal Today*, 1998, **41**, 207-219.
55. M. S. Dresselhaus, A. Jorio, M. Hofmann, G. Dresselhaus and R. Saito, *Nano Lett*, 2010, **10**, 751-758.
56. P. G. Mineo, L. Livoti, M. Giannetto, A. Gulino, S. Lo Schiavo and P. Cardiano, *J Mater Chem*, 2009, **19**, 8861-8870.
57. W. Fan, Q. Lai, Q. Zhang and Y. Wang, *J Phys Chem*, 2011, **115**, 10694-10701.
58. J. Yu, J. Jin, B. Cheng and M. Jaroniec, *Journal of Materials Chemistry A*, 2014, **2**, 3407-3416.
59. Q. Li, B. Guo, J. Yu, J. Ran, B. Zhang, H. Yan and J. R. Gong, *J Am Chem Soc*, 2011, **133**, 10878-10884.
60. W. J. Ong, L. L. Tan, S. P. Chai and S. T. Yong, *Chem Commun*, 2015, **51**, 858-861.
61. L. Shen, S. Liang, W. Wu, R. Liang and L. Wu, *Dalton Trans*, 2013, **42**, 13649-13657.
62. W. Liu, D. Sun, J. Fu, R. Yuan and Z. Li, *RSC Advances*, 2014, **4**, 11003-11011.
63. Y. Fu, D. Sun, Y. Chen, R. Huang, Z. Ding, X. Fu and Z. Li, *Angewandte Chemie*, 2012, **124**, 3420-3423.

Table of Contents Entry

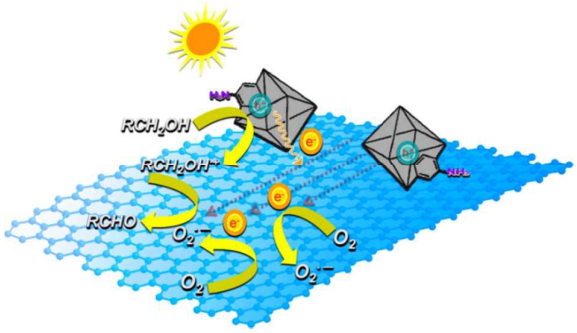

By employing noncovalent methodology, the hierarchical rGO/MOF hybrids were successfully fabricated to enhance the photocatalytic performance for the organic photosynthesis under visible light.